Three-Dimensional Study of Vortico-Acoustic Interaction in a Simulated Solid Rocket Motor

Hengyu Hu* and Ruipeng Tian†
University of Science and Technology of China, 230027 Hefei, Anhui Province, People's Republic of China
Dexin Wang‡ and Miao Ding‡
Xi'an Institute of Aerospace Solid Propulsion Technology, 710199 Xi'an, Shaanxi Province, People's Republic of China
and
Haibo Huang§
University of Science and Technology of China, 230027 Hefei, Anhui Province, People's Republic of China

https://doi.org/10.2514/1.J064387

In this study, a three-dimensional numerical simulation of a large length-diameter ratio solid rocket motor is carried out using the large-eddy simulation. Pressure oscillation excited by significant parietal vortex shedding (PVS) is observed. The acoustic feedback model is successfully extended to investigate the interaction between PVS and pressure oscillations, and the result proves that the model has sufficient accuracy (with 2.84% relative error) to predict the PVS frequency in an accelerating flow field. Reduced-order variational mode decomposition (RVMD) is performed to analyze the vorticity field, indicating that the method can identify the PVS frequency accurately (with 3.42% relative error) and capture large-scale vortex structures that remain intact at the rear of the combustion chamber. Based on RVMD and Hilbert spectral analysis, the framework of model-based time-frequency analysis is established and used to verify the stability of PVS frequency.

Nomenclature

a	=	sound speed, m/s
C_p	=	isobaric specific heat capacity, J/(kg · K)
C_w	=	Smagorinsky coefficient
c_k	=	time-evolution coefficient of kth mode; unit depends on flow data being decomposed
d_{v1}, d_{v2}	=	vortex spacing, m
E_{pp}	=	pressure spectra, Pa²/Hz
f_k	=	central frequency of kth RVMD mode, Hz
f_{nL}	=	nth intrinsic acoustic mode, Hz
f_s	=	sampling frequency, Hz
K	=	number of modes
L	=	chamber length, m
l	=	acoustic feedback distance, m
M	=	molar mass, kg/mol
m	=	stage number
$\dot{m}$	=	injection mass flow rate per unit area, kg/(s · m²)
n	=	order of intrinsic acoustic mode
p	=	pressure, Pa
R	=	ideal gas constant, J/(kg · K)
R_c	=	chamber radius, m
r	=	radial coordinate, m
S	=	Sutherland temperature, K
T_{inj}	=	injection temperature, K
T_{ref}	=	reference temperature, K
U	=	velocity magnitude, m/s
U_a	=	axial velocity magnitude, m/s
U_c	=	convection velocity, m/s
U_{inj}	=	injection velocity magnitude, m/s
U_r	=	radial velocity magnitude, m/s
u_i	=	velocity vector, m/s
χ	=	correction factor in Rossiter acoustic model
x	=	axial coordinate, m
α	=	filtering parameter, Hz⁻²
γ	=	specific heat ratio
Δ	=	bandwidth of filtering function, Hz
Δ_c	=	cell length, m
Δt	=	time delay, s
Δx	=	axial separation, m
ε_t	=	turbulent dissipation rate, m²/s³
η	=	Kolmogorov length, m
θ	=	azimuthal coordinate, rad
λ	=	heat transfer coefficient, W/(m² · K)
μ_{ref}	=	reference dynamic viscosity, (N · s)/m²
ν	=	kinematic viscosity, m²/s
ρ	=	density, kg/m³
ϕ_k	=	kth spatial mode
ω_z	=	vorticity about z axis, rad/s
ω_m	=	vorticity magnitude, rad/s

Subscripts and Superscripts

$(\cdot)_{rms}$	=	root mean square
$(\cdot)_b$	=	average flow property over given cross section of chamber
$\overline{(\cdot)}$	=	time or spatial average
$\tilde{(\cdot)}$	=	oscillation

*Master Degree Candidate, Department of Modern Mechanics.
†Doctoral Candidate, Department of Modern Mechanics.
‡Researcher, Xi'an Institute of Aerospace Solid Propulsion Technology.
§Professor, Department of Modern Mechanics; huanghb@ustc.edu.cn.

I. Introduction

SOLID rocket motors (SRMs) with large length–diameter ratios and high-energy propellants find extensive applications in tactical missiles, rockets, and various equipment. However, the combustion process in these SRMs often leads to flow instabilities, resulting in pressure oscillations [1]. This phenomenon involves the coupling of instabilities-generated vortexes which is dominated

by turbulent gas motions [2], with the intrinsic acoustic modes of the combustion chamber, leading to significant pressure fluctuations, commonly known as vortex-acoustic coupling [3]. This mutual coupling results in significant changes in the unsteady flow evolution [4]. Previous investigations [3,5] have identified three forms of vortex shedding responsible for inducing vortex-acoustic coupling in SRMs: corner vortex shedding (CVS), obstacle vortex shedding (OVS), and parietal vortex shedding (PVS). CVS and OVS typically occur in the presence of backward-facing steps or obstacle structures on the propellant surface, such as inhibitor rings or cavities between segments, triggered by Kelvin–Helmholtz instability. Conversely, PVS is linked to purely hydrodynamic instability [3]. Notably, even in SRMs lacking backward-facing steps or obstacle structures, PVS may occur, particularly in SRMs with substantial length–diameter ratios, where generated vortexes disperse away from the wall [6]. Following Lupoglazoff and Vuillot's pioneering work [6] on PVS, this phenomenon has garnered increasing attention from researchers. Avalon et al. [7] successfully identified PVS with injection at the wall, using planar laser induced fluorescence. Lupoglazoff and Vuillot [8] conducted direct numerical simulations of the oscillatory flow field in a laboratory cold flow setup based on two-dimensional (2D) unsteady compressible Navier–Stokes equations, demonstrating the crucial role of spatially distributed noise in driving PVS. Gazanion et al. [9] introduced Gaussian uncorrelated noise with zero mean to the injection velocity in their numerical simulation of PVS. Before this, researchers used VALDO (a cold flow experimental setup previously used to demonstrate the existence of PVS [10]) to study laminar-turbulent transition with PVS, obtaining a description of laminar and turbulent areas across the flow, from which a transition line was defined [11]. Similarly, Apte and Yang [12] characterized the overall flow development with surface mass injection by three distinct regimes: laminar, transitional, and fully turbulent flows. Recently, Li et al. [13] employed linear stability analysis to explore the cause of PVS in Taylor–Culick flow, highlighting the significant role of flow turning resulting from lateral mass injection in PVS formation. Furthermore, some scholars have investigated pressure oscillations induced by vortex shedding. Dotson et al. [14] used the acoustic feedback model developed by Rossiter [15] to analyze the Titan IV RSRM, elucidating the mechanism of pressure oscillations caused by vortex shedding. Flandro and Jacobs [16] proposed a straightforward acoustic feedback model for flow over rectangular cavities, suggesting that acoustic amplitude peaks when vortex shedding is coupled with the chamber's intrinsic acoustic modes.

In the realm of numerical simulations, early researchers primarily employed 2D simulations to investigate vortex shedding and pressure oscillations in SRMs [5,17–19]. Lupoglazoff and Vuillot [20] conducted 2D simulations of the Ariane 5 P230 MPS and found that the computational pressure oscillation level exceeded that of experimental observations. They inferred that this discrepancy might stem from 2D simulations inadequately capturing the transition of vortexes to small-scale turbulence. Therefore, conducting large-scale, high-fidelity three-dimensional (3D) simulations becomes imperative to accurately capture vortex breakdown and energy cascade phenomena. Large eddy simulation (LES), a widely used turbulence model, proves effective in simulating 3D vortex shedding with high precision [21,22], and it can accurately simulate the interaction between mean, turbulent, and acoustic flows [23]. As a trade-off, high-precision LES requires substantial computational resources [4]. Apte and Yang [24] used LES to investigate the unsteady flow evolution in a porous chamber with surface mass injection, simulating propellant burning in a nozzle-less solid rocket motor. They observed three successive flow development regimes: laminar, transitional, and fully developed turbulent flow. Bernardini et al. [22] employed implicit large-eddy simulation to conduct a 3D high-fidelity numerical simulation of the ONERA C1xb SRM and compared it with the frequency predicted by the acoustic feedback model developed by Rossiter [15]. More recently, Di Mascio et al. [25] used time-accurate LES to simulate a full-scale SRM and developed a new boundary condition to replicate the velocity and temperature fluctuations observed at the burning surface.

Turbulent flows are characterized by intense, nonlocal interactions among multiple degrees of freedom, resulting in spatial-temporal multiscale features [26]. High-precision three-dimensional simulations will lead to a dramatic increase in the amount of data, which can pose difficulties for subsequent analysis. Modal decomposition has become fundamentally important in turbulence research, offering a means to construct a low-dimensional (low-order) representation from an Eulerian perspective and establish an explicit connection between dynamic processes in physical and phase space [27]. Researchers often apply modal decomposition to flow physics to capture their essence [28]. The earliest modal decomposition method, proposed by Lumley [29], is the proper orthogonal decomposition (POD). Over the past 50 years, a series of modal decomposition methods, including POD and dynamic mode decomposition (DMD) [30], have been widely applied in theoretical and industrial fields [31]. POD and DMD enable the revelation of complex flow structures and frequency characteristics by analyzing a series of snapshots, which can be obtained through experiments or simulations [32–34]. For natural and periodically forced flows around 2D bluff bodies, DMD and POD offer insights into the effectuated changes by actuation through the decomposition of the velocity field [35]. The composition of a 2D velocity field using DMD can unveil flow separation near the backward-facing step in SRM [36]. Recently, researchers have integrated concepts from signal processing into modal decomposition, proposing new methods such as spectrum proper orthogonal decomposition and reduced-order variational mode decomposition (RVMD). Scholars have constructed an RVMD-based time-frequency analysis framework from the Hilbert view, effectively extracting characteristics from transient or statistically nonstationary flows. This framework also enables a quantitative understanding of dominant, representative, coherent components in complex flows [37]. As a contrast, POD identifies an orthonormal basis that captures the maximum variance in the data by projecting it onto a finite-dimensional subspace. When the filtering parameter α is set to zero, RVMD effectively becomes POD. Although both methods use similar optimization principles, RVMD offers the advantage of adaptively extracting low-order dynamics from time-spatial data, rather than just spatial or temporal features. Unlike POD, RVMD can handle nonstationary flows more effectively by integrating concepts from signal processing, such as the Hilbert transform, and introducing the concept of ELD [37]. DMD provides a global view of the system's spectral content but is limited by its exponential oscillatory formulation $e^{\lambda t}$, which may not adequately describe nonlinear or nonstationary processes, such as those with amplitude or frequency modulation. According to Liao et al. [37], RVMD is better suited for such complex processes. However, to date, there has been no research using RVMD to analyze PVS in SRM, which serves as a motivation for this study.

In this study, we present the results of a simulation investigating unsteady single-phase compressible flow within a SRM characterized by a large length-diameter ratio. We employed 3D LES to perform high-precision simulation of the flow field in the SRM. The relationship between PVS and pressure oscillations is revealed using the acoustic feedback model. The effectiveness and accuracy of RVMD in decomposing flow fields in SRM are validated. We use RVMD to unveil large-scale vortexes that have not fully dissipated and gain a deeper understanding of the time-frequency features of PVS. The paper is structured as follows: Sec. II offers a concise overview of the simulation and modal decomposition techniques. Section III details the case statement and computational setup. Section IV presents the results and discussion, whereas Sec. V summarizes the conclusions drawn from our findings. Additionally, the Appendix includes details on grid convergence and verification procedures conducted to ensure the accuracy of the computational results.

II. Computational Strategy and Modal Decomposition

This study numerically solves the three-dimensional compressible Navier–Stokes equations using the finite-volume method. The governing equations, which include consideration of fluid viscosity and heat conduction, are as follows [38]:

$$\frac{\partial \rho}{\partial t} + \frac{\partial(\rho u_j)}{\partial x_j} = 0$$

$$\frac{\partial(\rho u_i)}{\partial t} + \frac{\partial(\rho u_i u_j)}{\partial x_j} = -\frac{\partial p}{\partial x_i} + \frac{\partial \tau_{ij}}{\partial x_j}$$

$$\frac{\partial(\rho E)}{\partial t} + \frac{\partial(\rho E u_j)}{\partial x_j} = -\frac{\partial(p u_j)}{\partial x_j} + \frac{\partial(\tau_{ij} u_i - q_j)}{\partial x_j} \quad (1)$$

E is the total energy per unit mass, τ_{ij} and q_j are the viscous stress tensor and the heat flux vector, and p is calculated as the thermodynamic pressure through the ideal gas law. The relationship between shear stress and shear rate is linear:

$$\tau_{ij} = 2\mu\left(\frac{\partial u_i}{\partial x_j} + \frac{\partial u_j}{\partial x_i} - \frac{1}{3}\frac{\partial u_k}{\partial x_k}\delta_{ij}\right) \quad q_j = -\lambda\frac{\partial T}{\partial x_j} \quad p = \rho RT \quad (2)$$

δ_{ij} is the Kronecker delta, T is the temperature, and μ is the dynamic viscosity, which can be calculated using Sutherland's law:

$$\mu = \mu_{\text{ref}}\left(\frac{T}{T_{\text{ref}}}\right)^{3/2}\frac{T_{\text{ref}} + S}{T + S} \quad (3)$$

The wall-adapting local eddy (WALE) viscosity model is used as the subgrid-scale model in LES [39]:

$$\mu_t = \bar{\rho}C_w^2 U^{2/3}\frac{\left(S_{ij}^d S_{ij}^d\right)^{3/2}}{\left(\tilde{S}_{ij}\tilde{S}_{ij}\right)^{5/2} + \left(S_{ij}^d S_{ij}^d\right)^{5/4}}$$

$$S_{ij}^d = \frac{1}{2}\left(\frac{\partial\tilde{u}_i}{\partial x_k}\frac{\partial\tilde{u}_k}{\partial x_j} + \frac{\partial\tilde{u}_j}{\partial x_k}\frac{\partial\tilde{u}_k}{\partial x_i}\right) - \frac{1}{3}\frac{\partial\tilde{u}_k}{\partial x_k}\frac{\partial\tilde{u}_k}{\partial x_k}\delta_{ij}$$

$$\tilde{S}_{ij} = \frac{1}{2}\left(\frac{\partial\tilde{u}_i}{\partial x_j} + \frac{\partial\tilde{u}_j}{\partial x_i}\right) \quad (4)$$

This paper employs RVMD to analyze the computational results. Similar to other modal decomposition methods, RVMD constructs a low-dimensional (low-order) representation of space-time flow data $Q(\mathbf{x}, t)$. Spatial mode $\phi_k(\mathbf{x})$ and time-evolution coefficient $c_k(t)$ together constitute the kth mode:

$$Q(\mathbf{x}, t) \cong \sum_{k=1}^{K}\phi_k(\mathbf{x})c_k(t) \quad (5)$$

The inherent mode function (IMF) proposed by Huang et al. [40] has gained application in various time-frequency analysis techniques, such as the synchrosqueezed wavelet transform [41] and the empirical wavelet transform [42] as a kind of orthogonal base. In this paper, the time-evolution coefficient $c_k(t)$ of RVMD is represented in the following IMF:

$$c_k(t) = A_k(t)\cos\varphi_k(t) \quad (6)$$

It has a nondecreasing phase $\varphi_k(t)$ and a nonnegative envelope $A_k(t)$. As an amplitude-modulated frequency-modulated signal, IMF possesses the following properties: the envelope and the derivative of the phase $d\varphi_k/dt$ should vary much slower than the phase. Each IMF has a limited bandwidth and revolves around a specific frequency (referred to as the *central frequency* f_k, and the corresponding central angular frequency is $\omega_k = 2\pi f_k$). The RVMD applied to space-time flow data is essentially solving the following constrained optimization problem:

$$\min_{\{\phi_k(\mathbf{x}),c_k(t),c_k\}}\left\{\alpha\sum_{k}^{K}\left\|\partial_t\left[\left(\delta(t) + \frac{j}{\pi t}\right)*c_k(t)\right]e^{-j\omega_k t}\right\|_2^2\right.$$

$$\left. + \left\|Q(\mathbf{x},t) - \sum_{k}^{K}\phi_k(\mathbf{x})c_k(t)\right\|_F^2\right\}$$

$$\text{s.t. } \|\phi_k(\mathbf{x})\|_2^2 = 1 \quad (7)$$

The filtering parameter α determines the shape of the filters in RVMD. The relationship between the bandwidth Δ, defined as the distance between the two half-power frequency points (cutoff frequencies) of the filter, and the parameter α can be expressed as follows:

$$\Delta = f_s\sqrt{\left(2\sqrt{2} - 2\right)/\alpha} \quad (8)$$

By introducing Lagrange multipliers, the constrained optimization problem (7) is transformed into an unconstrained form and is then solved iteratively using the alternating direction method of multipliers [43,44]. The convergence of the iterations is determined by the residual ϵ at each step. The calculation is terminated when the residual is less than a predetermined threshold ε. Subsequently, the RVMD modes $\{\phi_k, c_k, f_k\}|_{k=1}^{K}$ are obtained:

$$\epsilon = \sum_{k=1}^{K}\frac{\|u_k^{n+1} - u_k^n\|_F^2}{\|u_k^n\|_F^2} \quad u_k^i = \phi_k^i c_k^i \quad (9)$$

Similar to POD [29,36], RVMD uses energy E_k to evaluate the contribution of each mode to the flow field. Because the ϕ_k is already normalized during the calculation, the energy of each mode E_k is represented by the L^2-norm of the c_k, and the energy ratio $\hat{E}_k$ is calculated to measure the relative energy intensity of each mode:

$$E_k = \|c_k(t)\|_t^2 \quad \hat{E}_k = \frac{E_k}{\sum_i^K E_i} \quad (10)$$

Thanks to the properties of IMF, the c_k and its Hilbert transform result constitute the analytic signal [45]. Therefore, the Hilbert spectrum analysis (HSA) [40] of c_k can provide a curve of instantaneous frequency $d\varphi_k/dt$ over time, revealing the time-frequency characteristics of modes. This is also the main content of the mode-based time-frequency analysis framework proposed by Liao et al. [37]. The algorithm of RVMD ispresented in the Appendix:

$$\hat{c}_k(t) = c_k(t) + jH[c_k(t)] = A_k(t)e^{j\varphi_k(t)}$$

$$\varphi_k(t) = \arctan\{H[c_k(t)]/c_k(t)\} \quad j = \sqrt{-1} \quad (11)$$

$$H[h(t)] = \frac{1}{\pi}\int_{-\infty}^{\infty}\frac{h(\tau)}{t - \tau}\,d\tau \quad (12)$$

III.   Case Description

Figures 1 and 2 depict the SRM and mesh used in this study, which is composed of a cylindrical combustion chamber and a nozzle. Gas is injected into the chamber from the propellant grain, accelerated to supersonic velocity through the throat, and finally expelled through the outlet. The combustion chamber has a diameter of 85 mm and a length of 1084 mm, with a length-to-diameter ratio of 12.75. The
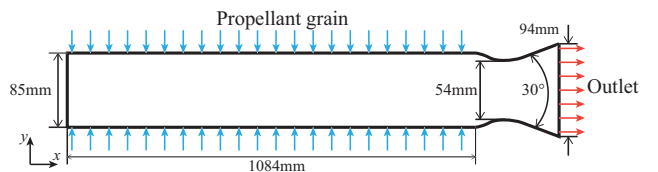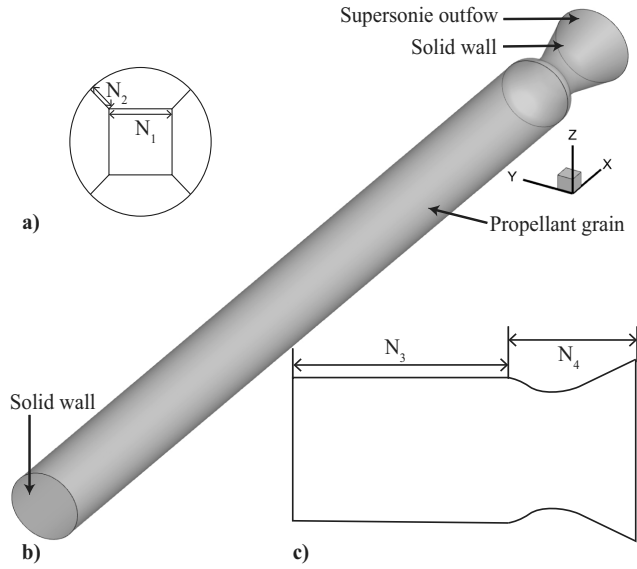

Fig. 1   Calculation model of SRM.

Fig. 2   a) and c) Mesh scheme of SRM. b) Three-dimensional visualization of the SRM.

Table 1   Physical values used for the simulation in this study

Parameter	Value
C_p, J/(kg · K)	2340
λ, W/(m · K)	0.0242
R, J/(kg · K)	287
γ	1.14
μ_{ref}, kg/(m · s)	$1.70 \cdot 10^{-5}$
T_{ref}, K	273
T_{inj}, K	$3.70 \cdot 10^3$
S, K	110
M, kg/mol	$2.90 \cdot 10^{-2}$
$\overline{m}$, kg/(s · m²)	44.5
$p_{t=0}$, MPa	9.00
$U_{inj,t=0}$, m/s	5.25
$Ma_{inj,t=0}$,	$4.77 \cdot 10^{-3}$
$\rho_{t=0}$, kg/m³	8.48
ς	0.200
C_w	0.325

throat of the nozzle has a diameter of 54 mm, with a contraction ratio of 2.48 and an expansion section with an angle of 15 deg. The outlet diameter is 94 mm.

Considering the focus of this study is on pressure oscillations, only single-phase ideal gas flow calculations without solid particles or molten metal droplets are performed. The grain regression due to combustion and erosion is not considered, so the geometrical configuration of the SRM is considered fixed during the computation. Chemical reactions and radioactive heat transfer phenomena are also not considered. These assumptions have been widely adopted in previous related studies [5,17,22,25]. The boundary conditions for the calculation are set as follows: the nozzle and the front end of the chamber are set as no-slip and adiabatic walls, the nozzle outlet is supersonic, and the surface of grain is a mass injection inlet with a specified flow rate $\dot{m}$ and temperature T_{inj}. Disturbances were added to the flow rate settings to promote the development of vortex shedding [8,9]. $\widetilde{m}$ is a Gaussian noise with a standard deviation of $\varsigma\overline{m}$ and mean of 0:

$$\dot{m} = \overline{m} + \widetilde{m} \tag{13}$$

$$N = (N_1 \cdot N_1 + N_1 \cdot N_2 \cdot 4) \cdot (N_3 + N_4) \tag{14}$$

O-grid blocking is used to generate a fully structured and wall-orthogonal grid consisting of N cells based on Eq. (14). The grid resolution changes in radial directions near the lateral wall, with a growth rate 1.1. A right-handed rectangular coordinate system is applied, with the origin located at the center of the front end of the chamber. The positive x axis points from the front end toward the outlet. Mesh independence and accuracy verification are presented in the Appendix, which proves that the fine mesh is suitable for the simulation in this study. The conversion relationship between cylindrical coordinates and rectangular coordinates is as follows:

$$x = x \quad r = \sqrt{y^2 + z^2} \quad \theta = \tan^{-1}(z/y) \tag{15}$$

The computational strategy adopted in this paper is as follows: first, the Reynolds-averaged Navier–Stokes is used for initial calculation with a time step of $\Delta t_1 = 1 \cdot 10^{-5}$ s, employing the $k - \omega$ SST turbulence model. When the flow field reaches a statistically stable condition, the calculated results are used as the initial flow field for the WALE-LES calculation, with a time step of $\Delta t_2 = 5 \cdot 10^{-6}$ s. Samples in a specific area have been recorded at $1 \cdot 10^{-5}$ intervals to guarantee sufficient resolution for analysis. The physical values used

for the simulation are reported in Table 1. The initial values of density $\rho_{t=0}$, pressure $p_{t=0}$, and injection velocity magnitude $U_{inj,t=0}$ are provided, and these physical quantities can be calculated in real time during the simulation through the ideal gas equation of state.

IV.   Result

A.   Flow Field Organization

This section illustrates the instantaneous and time-averaged of several substantial quantities to present the flow structure. As shown in the Fig. 3a, lateral injection results in a steady characteristic that manifests as the velocity heterogeneity in the axial direction, characterized by acceleration downstream. Figure 3b shows that the velocity within the chamber is significantly less than the speed of sound, indicating that the compressibility in this region can be neglected. The dimensionless fluctuation amplitudes describe the statistical characteristics of velocity, as shown in Fig. 4. A small peak in fluctuation amplitude is noticeable near the chamber's front, likely attributed to the no-slip boundary conditions, resulting in slight vortex shedding at the leading edge. As vortexes dissipate gradually due to viscosity, a stable laminar flow is established within the region 0.1 (m) < x < 0.65 (m). Beyond 0.65 (m), the fluctuation amplitude near the grain ($r/R_c = 0.9$) gradually increases, reaching a plateau at $x = 0.8$ (m). Similar trends are observed for different radial positions, aligning with the findings of Gazanion et al. [11] and Dunlap et al. [46], further elucidating the turbulent development within the chamber. Instantaneous vorticity contours (Fig. 5) and turbulent structures (Fig. 6), extracted using the Q criterion isosurface [47], corroborate these observations. Downstream, vorticity intensifies near the grain, leading to the appearance of annular rollers around $x = 0.65$ (m), indicative of vortex generation due to instability. These rollers progressively grow downstream, eventually transitioning into larger-scale vortexes by $x = 0.8$ (m), marking the onset of fully turbulent flow owing to energy cascade phenomena. The simulated vortex shedding aligns with previous studies on PVS [2,3], affirming its occurrence within the chamber. This analysis delineates three distinct regions within the chamber: Region I spans 0 (m) < $x \le 0.65$ (m), Region II encompasses 0.65 (m) < $x \le 0.8$ (m), and Region III extends from 0.8 (m) < $x \le 1.084$ (m). This is consistent with the analysis results of [12].

B.   Analysis of Pressure Oscillations

This section employs Fourier transform-based frequency analysis to scrutinize the characteristics of pressure oscillations across different frequencies and spatial distributions within the chamber. Eight strategically positioned monitoring points (MP1–MP8) were chosen
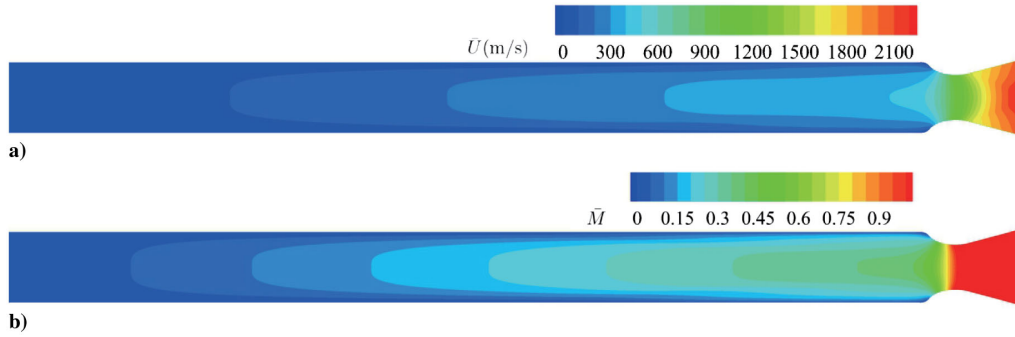
Fig. 3 Contours of time-averaged a) axial velocity and b) Mach number in xz plane located in $y = 0$ (m).
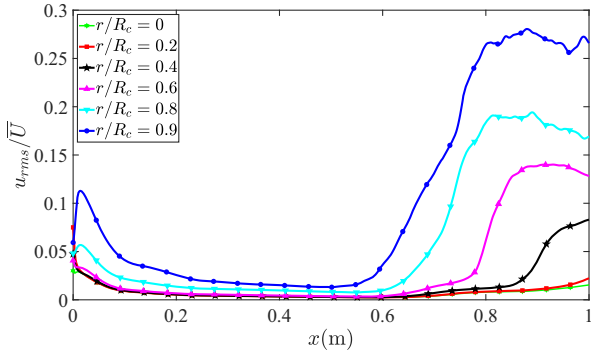

Fig. 4 Fluctuations intensities of axial velocity in chamber.

Table 2 Location of monitoring points in SRM

	MP1	MP2	MP3	MP4	MP5	MP6	Mp7	MP8
Region	I	I	I	II	II	II	III	III
x, (m)	0.55	0.60	0.65	0.70	0.75	0.80	0.85	0.90
y, (m)				0				
z, (m)				-0.035				

in Table 2. Instantaneous pressure data at these points were meticulously recorded.

Owing to the flow's axial heterogeneity induced by PVS, the time-averaged and oscillation amplitudes of pressure at these monitoring points exhibit significant variations, as depicted in Fig. 7. As the flow progresses downstream, a noticeable reduction in time-averaged pressure is observed, compared to a substantial increase in pressure oscillation amplitudes at points within Regions II and III. This decline in time-averaged pressure can be attributed to fluid acceleration, whereas the surge in pressure oscillations is directly linked to the presence of PVS.

To further investigate the frequency characteristics of pressure oscillations, we sampled the pressure along a monitoring line on the grain ($y = 0$ (m), $z = -0.0425$ (m), 0.05 (m) $\leq x \leq 1.08$ (m)). Subsequently, spectrum analysis was performed on the collected data to reveal the frequency and spatial distribution of pressure oscillation energy. The spatial resolution was set at 1.53×10^{-3} (m) and the frequency resolution at 25 Hz. Calculation used the Welch method, whereas a flat-top window function was applied for truncation with 50% overlap. Figure 8 depicts the main acoustic mode, predominantly situated in Region II, corresponding to the previously discussed PVS. The frequency band exhibits a bandwidth of approximately 600 Hz, and its central frequency is 1900 Hz. Considering its spatial correlation with PVS in the flow, this acoustic mode ($f = 1900$ Hz) is designated as the PVS frequency.

For comparison, the intrinsic acoustic modes of SRM are evaluated. According to classical acoustic theory, the acoustic wave equation can be expressed as
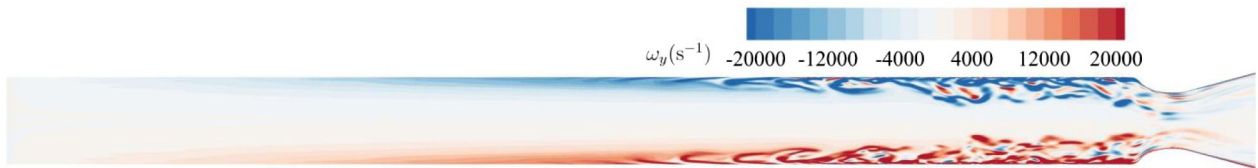

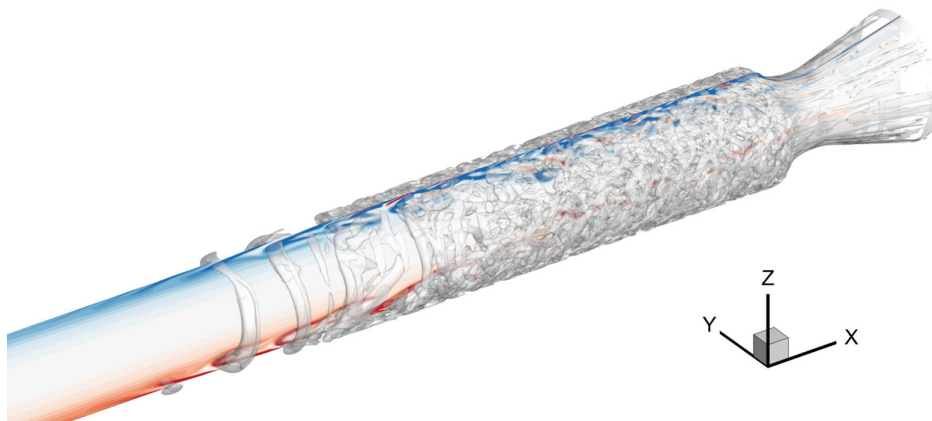**Fig. 5 Contours of instantaneous ω_y in longitudinal xz plane located in $y = 0$ (m).**

Fig. 6 Visualization of instantaneous turbulent structures through an isosurface of the Q criterion, $Q = 8 \cdot 10^5$ (s^{-1}).
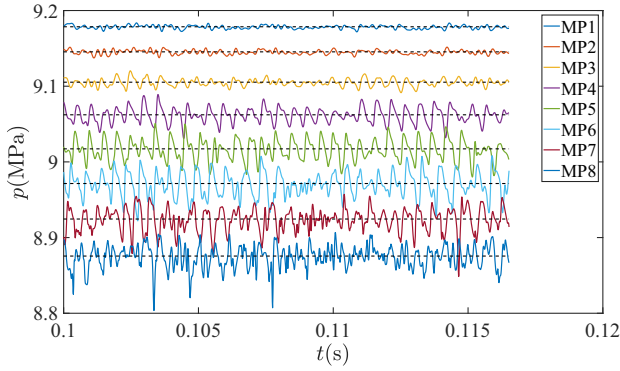
Fig. 7   Pressure-oscillation signals extracted from MP1 to MP8.

$$\frac{1}{a^2}\frac{\partial^2 \tilde{p}}{\partial t^2} - \nabla^2 \tilde{p} = 0 \qquad (16)$$

Pressure oscillations $\tilde{p}/\overline{p} \ll 1$ is satisfied, and the one-dimensional assumption is adopted in the cylindrical chamber, so the pressure oscillations have the following form:

$$\tilde{p} = P(x)e^{2j\pi ft} \qquad (17)$$

By substituting Eq. (17) into Eq. (16) and using the standing wave solution, the frequency of intrinsic acoustic modes of the SRM combustion chamber can be expressed as

$$f_{nL} = \frac{n\sqrt{\gamma RT}}{2L} \qquad (18)$$

The acoustic mode order, denoted as n, is represented by a positive integer, whereas the distance from the front end of the combustion chamber to the throat of the nozzle is $L = 1.156$ (m). In Fig. 8, the first four orders of intrinsic acoustic modes $f_{1L} \sim f_{4L}$ are delineated by dashed lines, corresponding to frequencies of 475, 951, 1427, and 1904 Hz, respectively. These markings align with findings from prior research on pressure oscillations in SRM [7,8,22,48–50], indicating a coupling between vortex shedding and the intrinsic acoustic mode. Within Region III, the pressure oscillation bandwidth progressively widens, accompanied by the disappearance of lower frequency components. This phenomenon signifies the breakdown of vortex

structures and the energy cascade from a frequency standpoint. As the flow transitions toward fully turbulent conditions, small-scale turbulence characterized by high oscillation frequency and broad bandwidth becomes increasingly prominent.

C.   Vortex-Acoustic Coupling

A more profound comprehension of pressure oscillations can be achieved by scrutinizing the correlation between pressure over time and space and the coherent structures generated by PVS. The space-time correlation coefficient of pressure oscillations is defined as follows:

$$C_{pp}(x, \Delta x, \Delta t) = \frac{\overline{\tilde{p}(x,t)\tilde{p}(x+\Delta x, t+\Delta t)}}{\left[\overline{\tilde{p}^2(x,t)}\right]^{1/2}\left[\overline{\tilde{p}^2(x+\Delta x, t+\Delta t)}\right]^{1/2}} \qquad (19)$$

$$U_c(x, \Delta x) = \frac{\Delta x}{\underset{\Delta t}{\arg\max}[C_{pp}(x, \Delta x, \Delta t)]} \qquad (20)$$

Δx and Δt represent the spatial separations in the axial directions and the time delay, respectively. The overbar indicates averages taken over time. C_{pp}, as depicted in Fig. 9, is derived from the monitoring line established on the grain ($r = R_c$). In Region II, the coherent structures manifest as distinct alternating strips of high positive and negative correlation, indicating that the vortexes convey pressure information downstream. As these strips formed upstream break down, the stable, coherent structures within the pressure field vanish, resembling the typical structures observed in turbulent boundary layers [48,51]. Analyzing the strips in Region II can help unveil the spatial distribution and movement patterns of vortexes within the chamber. Following Refs. [22,52], the convective velocity U_c of vortexes is defined as the ratio of the spatial interval to the time delay at which the correlation coefficient reaches a positive peak. The plot in Fig. 10 illustrates the relationship between local convective velocity U_c and interval Δx at a specific axial position. It is observed that when Δx is sufficiently small, the local U_c remains nearly constant. Furthermore, the graph in Fig. 10 demonstrates a general trend of increasing local U_c along the downstream direction. This phenomenon arises from flow acceleration with lateral injection, where the axial velocity of the flow field continuously increases along the axial direction. Because at $\Delta t = 0$ (s), the two consecutive peaks in Fig. 9 can be used to estimate the local vortex spacing [22], an alternative contour of the correlation coefficient is presented in Fig. 11, calculated
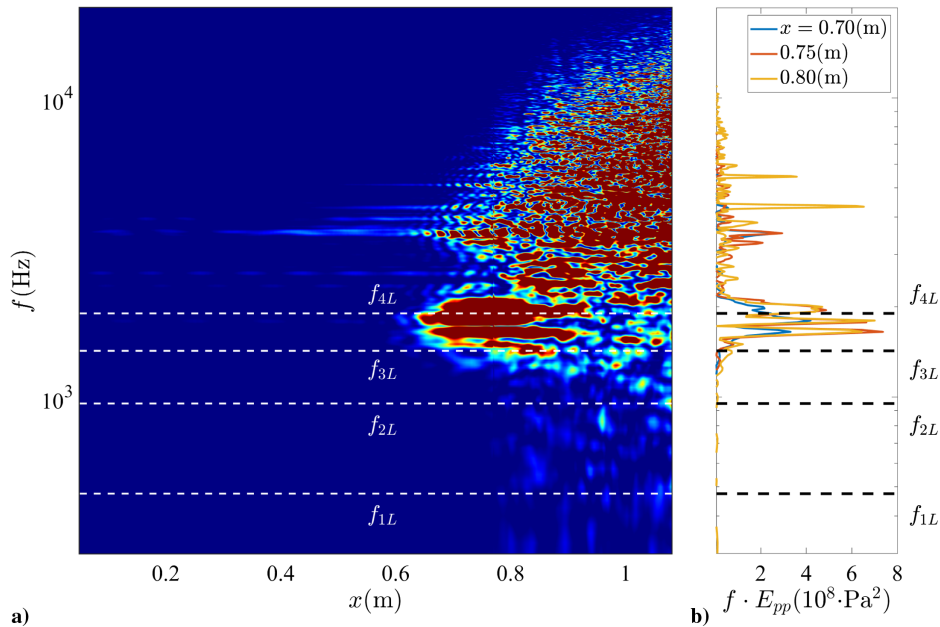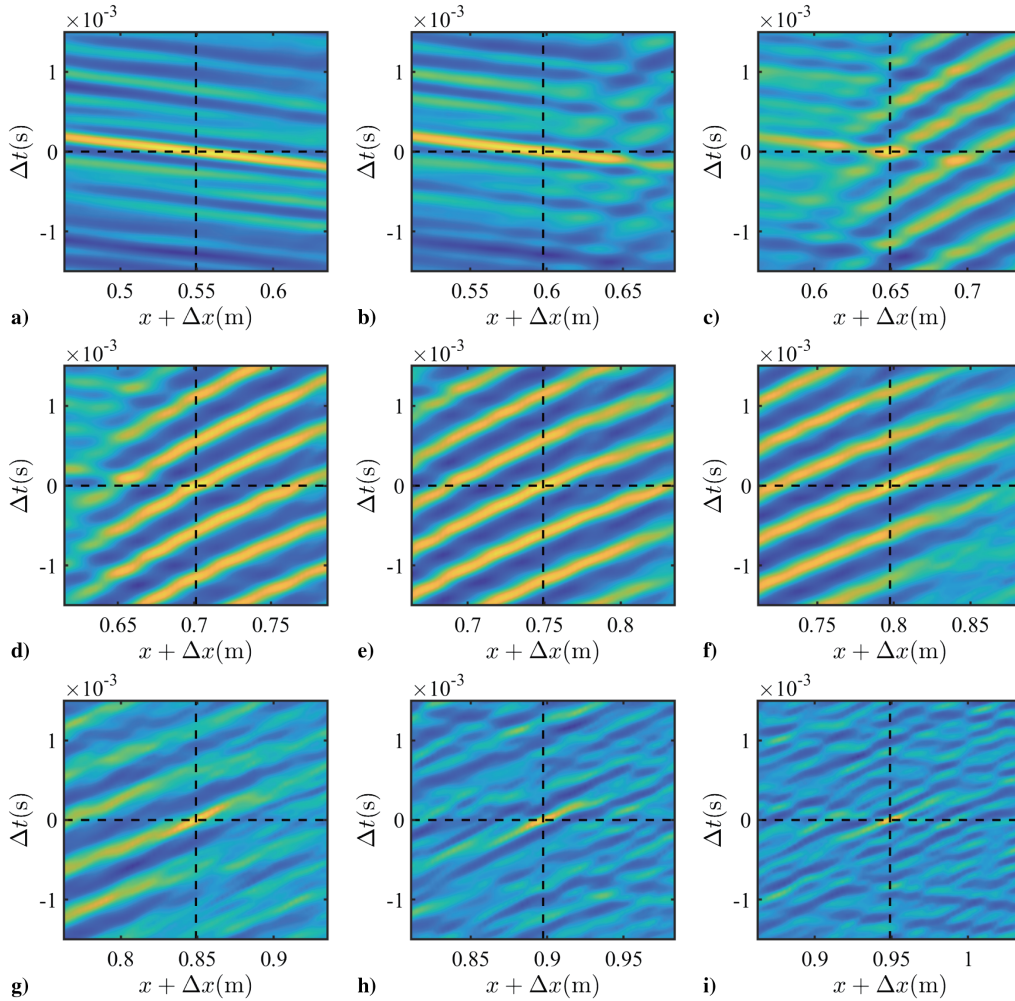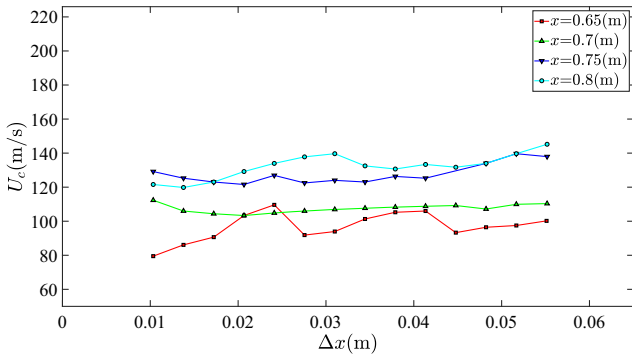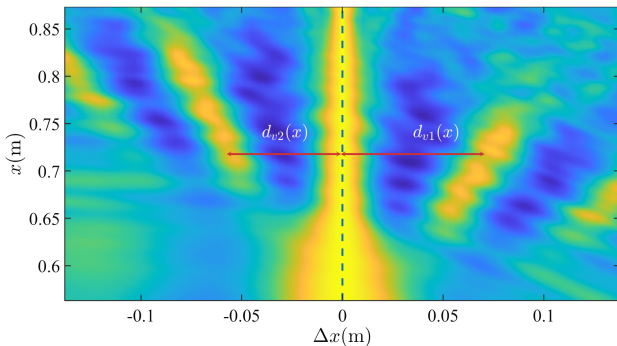

Fig. 8   a) Contour of pressure signals' spectrum on grain. b) Slices at specific axial location.

Fig. 9 Contours of space-time pressure correlation coefficient at different axial location.

Fig. 10 Local convection velocity of the eddies.

Fig. 11 Contours of space pressure correlation coefficient.

by Eq. (19) with $\Delta t = 0$ (s). The positive peaks in the correlation coefficients on both sides reflect the asymmetric distribution of vortexes along the axial direction induced by PVS. In Region I, the positive peaks only appear at $\Delta x = 0$ (m) and $\Delta x > 0$ (m), indicating a significant local and downstream vortex structure. The distance between the two positive peaks indicates the spacing between the vortex at this position and the next vortex downstream. Moving downstream, in Region II, the positive peak at $\Delta x < 0$ (m) suggests that the vortex is generated upstream. Meanwhile, the increasing vortex spacing with position is attributed to the difference in convective velocity between adjacent vortexes. In Region III, the downstream vortexes begin to break down, resulting in only the observation of the upstream positive peak. The downstream and upstream vortex spacings in x are denoted as $d_{v1}(x)$ and $d_{v2}(x)$, respectively. A detailed definition of $d_{v1}(x)$ and $d_{v2}(x)$ can be depicted in Fig. 12. It should be noted that $d_{v2}(x)$ cannot be defined in Region I, as the vortexes have not yet been generated upstream. Similarly, $d_{v1}(x)$ cannot be defined at Region III. Because of the downstream acceleration $d_{v1}(x)$ is always greater than $d_{v2}(x)$, which results in the *yellow thick lines* in Fig. 11 not being parallel.

It is worth exploring the accuracy of the acoustic feedback model developed by Rossiter [15] in calculating the PVS frequency in the flow with lateral injection after analyzing the characteristics of pressure oscillations. Dotson et al. [14] extended Rossiter's model to SRM, dividing the entire process into four parts: 1) vortexes are generated at a certain position and move along the downstream direction. 2) Vortexes strike the boundary (in this case, the contraction section of the nozzle) at a certain frequency, causing acoustic disturbance. 3) The disturbance propagates upstream. 4) The disturbance reaches the vortex shedding location and then triggers new
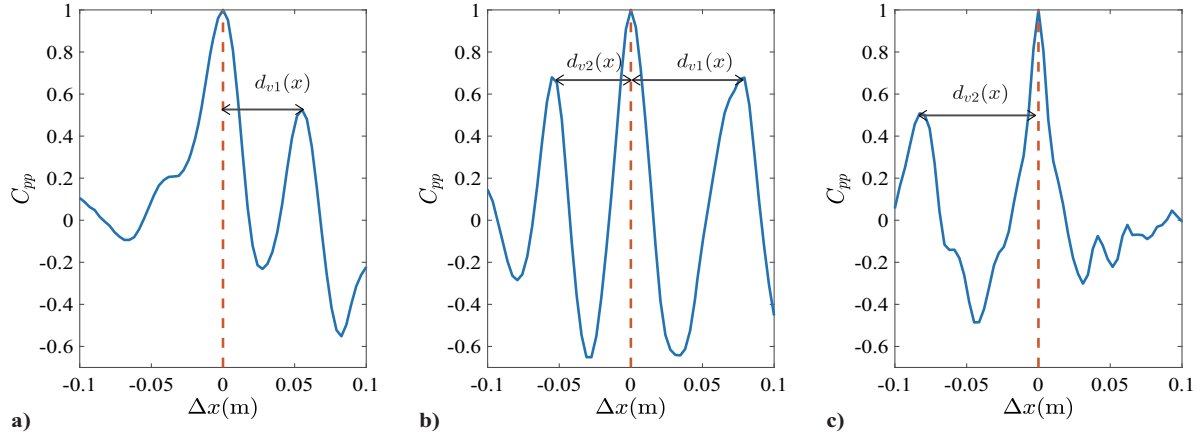
Fig. 12 Definition of $d_{v1}(x)$ and $d_{v2}(x)$ in a) $x = 0.65$ (m), b) $x = 0.72$ (m) and c) $x = 0.84$ (m).

vortex shedding, closing the feedback loop. In this process, the acoustic feedback frequency f_{AM} can be expressed as Eq. (21) [53,54]:

$$f_{AM} = \frac{d_v^{-1} - \chi/l}{1/U_c + 1/a} \qquad (21)$$

The correction factor χ is employed to rectify the time lag between vortex impact and the generation of acoustic disturbance [14], with a range from 0 to 25, as documented in [22]. The acoustic feedback distance l is defined as the distance from the vortex shedding position at $x = 0.650$ (m) to the impact point at $x = 1.08$ (m). In this investigation, $\chi = 0$, $l = 0.43$ (m), and $a = 1100$ (m/s). As previously mentioned, both the spacing between vortexes and the convective velocity vary considerably along the axial direction. Hence, the averages of vortex spacing $\bar{d}_v(x)$ and convective velocity $\overline{U}_c(x)$ are defined as Eq. (22), where δx is an integral parameter which is much smaller than $d_{v1}(x)$ and $d_{v2}(x)$:

$$\bar{d}_v(x) = \begin{cases} \dfrac{1}{\delta x}\displaystyle\int_{x-\delta x/2}^{x+\delta x/2} d_{v1}(\tau)\,\mathrm{d}\tau & x \in \text{Region I} \\[2ex] \dfrac{1}{2\delta x}\displaystyle\int_{x-\delta x/2}^{x+\delta x/2} [d_{v1}(\tau)+d_{v2}(\tau)]\,\mathrm{d}\tau & x \in \text{Region II} \\[2ex] \dfrac{1}{\delta x}\displaystyle\int_{x-\delta x/2}^{x+\delta x/2} d_{v2}(\tau)\,\mathrm{d}\tau & x \in \text{Region III} \end{cases}$$

$$\overline{U}_c(x) = \frac{1}{\delta x}\int_{x-\delta x/2}^{x+\delta x/2} U_c(\tau)\,\mathrm{d}\tau \qquad (22)$$

The simulated and linear fitting results at various positions are depicted in Fig. 13. The slope derived from the fitting denotes the
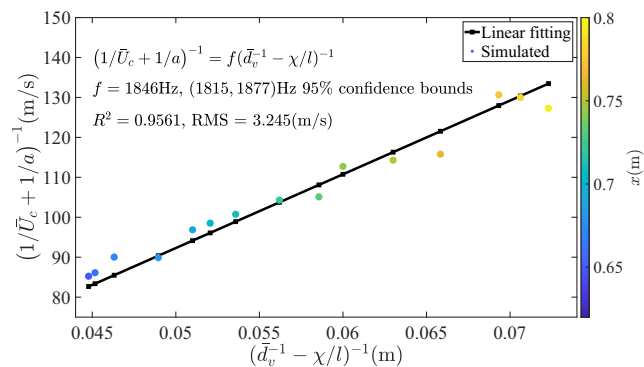

Fig. 13 Verification of acoustic feedback model, where points are colored by their axial position.

acoustic feedback frequency, which closely aligns with the predicted PVS frequency discussed earlier. Clearly, the acoustic feedback model maintains a high level of accuracy in forecasting the PVS frequency in accelerated flow. Furthermore, it highlights that the pressure oscillation frequency remains constant with position during PVS, consistent with the spectrum analysis findings. However, despite examining vorticity contour, Q-criterion, or spectrum analysis of pressure oscillations on the grain, no significant large-scale vortexes were observed in Region III. Thus, the acoustic feedback model still exhibits limitations in elucidating PVS frequency. In the subsequent section, RVMD is used to further analyze the spatial distribution of large-scale vortexes generated by PVS.

D. Reduced-Order Variational Mode Decomposition

To gain a deeper insight into PVS, RVMD is applied to the y-direction vorticity ω_y at the xz plane positioned at $y = 0$ (m). The range along the axial direction spans from 0.05 (m) to 1.08 (m), comprising 299 points. Along the z direction, the range extends from -0.0425 (m) to 0 (m), with 43 points. A total of 700 flow snapshots are selected with a sampling interval of $2 \cdot 10^{-5}$ (s), providing a frequency resolution of 71.42 (Hz). Consequently, the total data volume amounts to $299 \times 44 \times 700 = 8{,}999{,}900$. The choice of filter parameters significantly influences the results of RVMD [37]. If the filter parameter α is too small (resulting in a wide filter bandwidth Δ), individual modes in the RVMD may encompass multiple characteristic frequencies, diminishing their interpretability. Conversely, an excessively large α (narrow Δ) can reduce RVMD's adaptability, potentially leading to a filter bandwidth smaller than the frequency resolution. Table 3 illustrates the relationship between filter parameters and their corresponding filter bandwidths, expressed in both hertz and sampling points. Based on the bandwidth obtained from spectrum analysis in Sec. IV.B, α is set to 23011 (Hz^{-2}), with $\Delta = 600$ (Hz).

In determining the number of modes K, trial calculations are employed to assess the impact of K on decomposing the vorticity field, with convergence residuals set to $\varepsilon = 10^{-3}$. Figure 14 showcases the central frequency and energy ratio of each mode under different K values, elucidating how K influences RVMD outcomes. Overall, RVMD exhibits a strong capability to capture flow characteristics. Without prior information (uniform initialization of central frequencies), the modes tend toward characteristic frequency bands, except in instances where K is too small. In such scenarios, insufficient modes result in inaccurate calculation of the central frequency

Table 3   **Filtering parameters α and the corresponding filter bandwidths Δ**

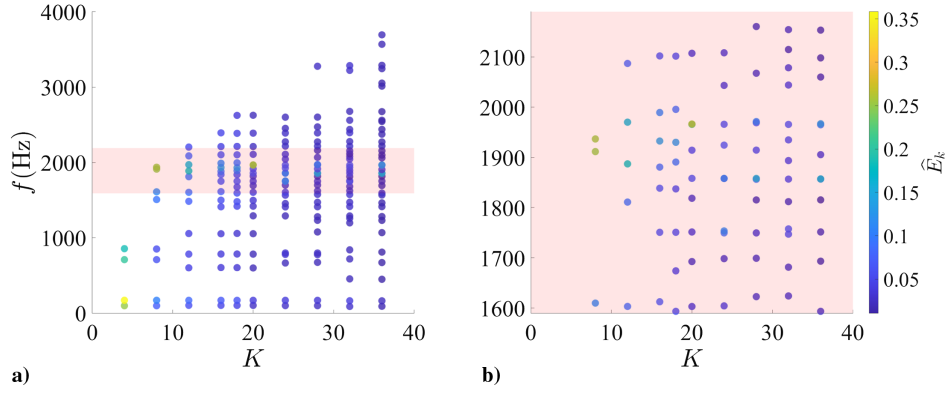| α, Hz^{-2}	2537667	101506	23011	4060	649
Δ, (Hz)	57	286	600	1428	3571
Δ, (Points)	0.8	4	8.4	20	50

Fig. 14   a) RVMD results under different K include the central frequency and energy ratio. b) Partial enlargement of a).

of the mode. For instance, when $K = 4$, RVMD fails to analyze any mode with a central frequency within the characteristic frequency band. Increasing K significantly improves this situation, although larger K values may adversely affect calculation and convergence speeds. Consequently, RVMD parameters are set to $K = 20$ for subsequent formal calculations, with convergence residuals set to $\varepsilon = 10^{-5}$ to ensure accuracy.

The central frequency and energy ratio distribution of the modes obtained from the RVMD are depicted in Fig. 15. Modes 15 and 16 exhibit a notable advantage in energy ratio, with their central frequencies closely aligned at 1964 (Hz) and 1966 (Hz), respectively. When the result of spectrum analysis is used as the standard, the relative errors of the acoustic model and RVMD are 2.84 and 3.42%, respectively. To explore the relationship between these two modes, we computed the cross correlation $R_{k'k}$ and the corresponding phase lag $\Delta\varphi_{k'k}$ of the c_k.

The highest correlation was observed between modes 15 and 16, with a corresponding phase lag $|\Delta\varphi_{15,16}| = |\Delta\varphi_{16,15}| \approx \pi$, resembling the anti-phased modes in Fourier analysis. Given their substantial correlation and the absolute advantage in energy ratio over other modes, modes 15 and 16 are denoted as a pair of primary modes:

$$R_{k'k} = \frac{\max_\tau \int_{-\infty}^{\infty} c_k(t)c_{k'}(t+\tau)\,\mathrm{d}t}{\sqrt{\int_{-\infty}^{\infty} |c_k(t)|^2\,\mathrm{d}t}\sqrt{\int_{-\infty}^{\infty} |c_{k'}(t)|^2\,\mathrm{d}t}} \quad (23)$$

$$\Delta\varphi_{k'k} = 2\pi f_k\tau \qquad \tau = \arg\max_\tau \left\{\int_{-\infty}^{\infty} c_k(t)c_{k'}(t+\tau)\,\mathrm{d}t\right\} \quad (24)$$

Figure 16 illustrates the spatial distribution of the primary modes. In most regions of the flow field, the discrepancies between the
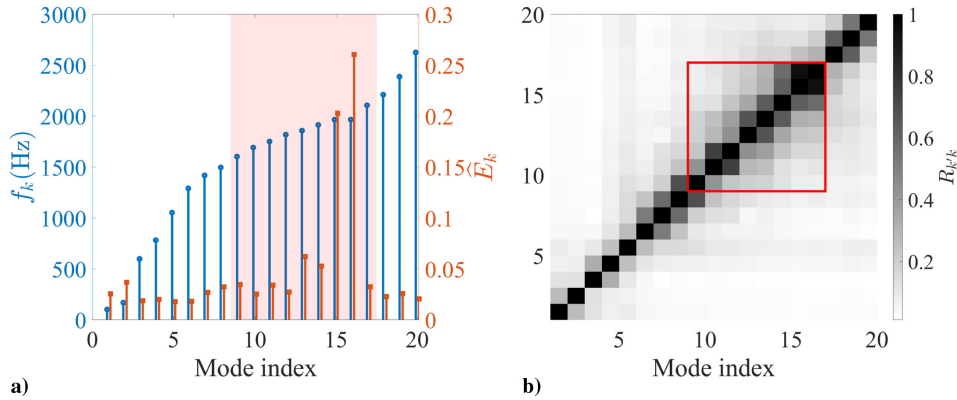

Fig. 15   a) Central frequency and energy ratio of each mode; the red box is the PVS frequency band. b) Maximum cross-correlation coefficient of the modes.
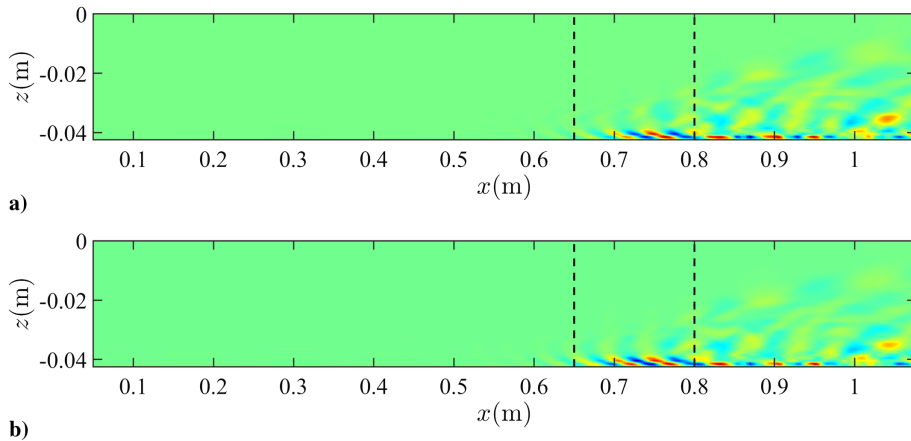

Fig. 16   Spatial distribution of the primary spatial modes in xz plane with $y = 0$ (m): a) ϕ_{15} and b) ϕ_{16}.
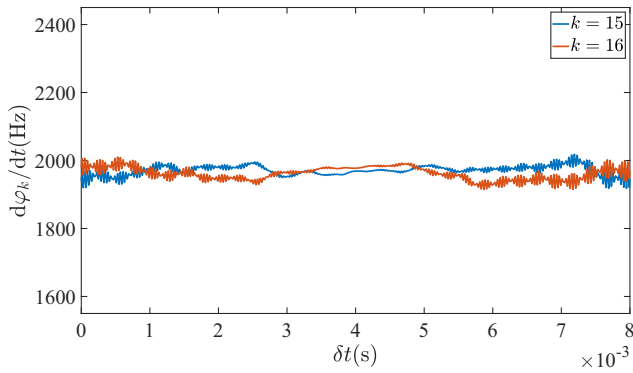
Fig. 17 Instantaneous frequency of the primary modes.

primary modes are minimal. Along the axial direction, the spatial distribution alternates between high and low values, gradually increasing in Region II before rapidly decreasing, although it remains significantly elevated compared to the background. When observed along the z direction, the primary modes initially emerge near the grain and progressively extend into the interior of the flow as their amplitudes increase.

From a spatial distribution and central frequency perspective, the primary modes decomposed by RVMD exhibit striking similarities to the PVS analysis results discussed earlier. Regarding frequency, the central frequencies of these primary modes predominantly cluster around 1965 Hz, aligning closely with the characteristic frequency band identified through pressure spectrum analysis and corresponding well with the PVS frequency prediction from the acoustic feedback model, with an acceptable margin of error. Spatially, the positions of the primary modes closely align with the determined PVS locations based on flow field analysis; their radial distribution characteristics also correspond to vortex growth patterns. Additionally, in Region III, the spatial distribution of primary modes exhibits a declining trend, progressively diffusing into the flow interior, reflecting the observed breakdown of vortexes in the spatial-temporal correlation analysis.

However, contrary to previous analyses, RVMD unveils large-scale vortexes that have not fully dissipated, many of which have detached from the grain. These structures impact the nozzle at specific frequency, generating acoustic disturbances that propagate upstream, initiating PVS and completing the acoustic feedback loop. Consequently, the RVMD results support the acoustic feedback model's explanation of PVS.

Earlier pressure spectrum analyses have demonstrated the coupling between PVS and the intrinsic acoustic mode of the chamber. As discussed in previous research, when the frequencies are coupled in flow fields undergoing OVS, a distinct *lock-in* phenomenon occurs, resulting in a constant frequency of pressure oscillations caused by vortex shedding. Given that previous sections have established PVS as the direct driver of pressure oscillations under these conditions, time-frequency analysis of vorticity can further aid in analysis and investigate the occurrence of *lock-in* in PVS.

The spatial modes ϕ_k and their corresponding time evolution coefficients c_k, decomposed from the vorticity field through RVMD, unveil the temporal and frequency characteristics of the modes. By appropriately selecting IMF, conducting HSA solely on c_k suffices to discern the central frequency trend over time, as proposed in the *Time-Frequency Analysis Based on RVMD* by Liao et al. [37]. The HSA results on the time evolution coefficients of the primary modes during a time period, depicted in Fig. 17, reveal that the PVS frequency remains stable over time, validating its temporal consistency coupled with the intrinsic acoustic mode.

V. Conclusion

In this study, the flow field in a large length-diameter ratio SRM is presented using a single-phase three-dimensional compressible Navier–Stokes equations and LES method. Visualizations based on vorticity and the Q-criterion revealed that the PVS appear in the SRM, preliminarily displaying the generation, development, and breakdown of large-scale vortexes. Meanwhile, pressure spectrum analysis revealed a primary acoustic mode on the grain, whose main spatial distribution highly coincided with the region of PVS, suggesting a potential association with vortex shedding. Calculations of the chamber's intrinsic acoustic modes indicated that it is coupled from the PVS frequency. Spatial-temporal correlation analysis of pressure further revealed the evolution process of vortexes caused by PVS and validated the accuracy of Rossiter's acoustic feedback model in predicting the PVS frequency in accelerating flow. Finally, the analysis of the vorticity field using RVMD demonstrated the method's capability to significantly reduce data volume while capturing the spatial, frequency, and temporal characteristics of the flow field effectively. 1) In the RVMD results of the vorticity field, the spatial distribution of the primary modes accurately captured the generation, development, and breakdown of vortexes in PVS and also captured large-scale vortexes that were not fully broken at the rear of the chamber, further validating the physical accuracy of the acoustic feedback model. 2) By the adaptive determination, RVMD accurately captured the frequency of the PVS. 3) Based on RVMD and conventional signal processing techniques, a modal-based time-frequency analysis framework naturally emerged in the Hilbert perspective, which verifies temporal steadiness of the PVS frequency.

Appendix A: Berman Equation and Taylor–Culick Solution

Berman [55] proposed the equation for flow in a circular chamber with lateral injection, and the viscous effects are represented by the defined injection Reynolds number Re_s:

$$\left[\left(\frac{F'}{r_0}\right)\left(\frac{F'}{r_0}\right)' - \left(\frac{F'}{r_0}\right)^2\right]' + \frac{1}{Re_s}\left[\frac{1}{r_0}\left(r_0\left(\frac{F'}{r_0}\right)'\right)'\right]' = 0$$

$$\left.\left(\frac{F'}{r_0}\right)'\right|_{r_0\to 0} = \left.\left(\frac{F}{r_0}\right)\right|_{r_0\to 0} = F'|_{r_0\to 0} = 0 \qquad F|_{r_0\to 1} = 1 \quad \text{(A1)}$$

$$\overline{\Phi} = xF(r_0) \quad \overline{U}_a = \frac{1}{r_0}\frac{\partial\overline{\Phi}}{\partial r_0} \quad \overline{U}_r = -\frac{1}{r_0}\frac{\partial\overline{\Phi}}{\partial x} \quad r_0 = \frac{r}{R_c} \quad \text{(A2)}$$

$$Re_s = \frac{2\rho\overline{U}_{inj}R_c}{\mu} \qquad Re_c = \frac{2\rho\overline{U}_aR_c}{\mu} \quad \text{(A3)}$$

The Berman equation can yield the Taylor–Culick solution [56,57] for cases with $Re_s \to \infty$. Experimental and numerical studies have validated this flow pattern, and it is known for its strong robustness [58–61]. Under the conditions of $Re_s > 100$, the Berman equation shows little difference from the Taylor–Culick solution [11]. At the same time, it only deviates significantly from actual flows at axial flow Reynolds number meets $Re_c > 10^5$ [22]. The velocity field calculated by the Taylor–Culick solution is as follows:

$$\overline{U}_a = \pi\frac{x}{R_c}\overline{U}_{inj}\cos\left[\frac{\pi}{2}\left(\frac{r}{R_c}\right)^2\right] \qquad \overline{U}_r = -\frac{R_c}{r}\overline{U}_{inj}\sin\left[\frac{\pi}{2}\left(\frac{r}{R_c}\right)^2\right] \quad \text{(A4)}$$

Appendix B: Mesh Independence

Three types of mesh were constructed in this study, and their parameters are listed in Table B1. The comparison between approximate Kolmogorov length η [62] and cell length Δ_c is presented to

Table B1   Summary of the mesh setting

	N1	N2	N3	N4	η/Δ_c
Fine mesh	38	50	710	86	$O(10^{-1})$
Medium mesh	34	46	670	80	$O(10^{-2})$
Coarse mesh	29	40	648	66	$O(10^{-2})$
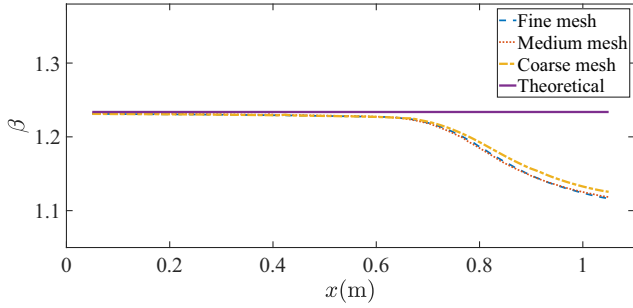
Fig. B1 Axial variations of momentum flux coefficient β.

demonstrate the mesh's reasonable resolution for turbulence. The comparison is primarily focused on Region III. Equation (B1) uses the relations $\varepsilon_t \approx \mu\omega_m^2$ and $\nu = \mu/\rho$. ε_t is the turbulent dissipation rate, ν is the kinematic viscosity, and ω_m is the vorticity magnitude:

$$\eta = \left(\frac{\nu^3}{\varepsilon_t/\rho}\right)^{1/4} \sim \left(\frac{\mu^2}{\rho^2\omega_m^2}\right)^{1/4} \tag{B1}$$

The momentum flux coefficient β for the SRM flow field under different grids was calculated, which can reflect the flow transition [24]. The variation of β in the combustion chamber under different mesh with axial coordinates is shown in Fig. B1. The theoretical results are calculated based on the Taylor–Culick solution. When calculating β based on the theoretical solution, assuming that the time-averaged density is uniform over the $r\theta$ plane, which means $\overline{\rho}(x,r,\theta) = \overline{\rho}_b(x)$, β obtained from the theoretical solution will not change with the axial position due to the velocity distribution characteristics. But β undergoes significant changes in the simulation due to turbulence [24]:

$$\beta(x) = \int_0^{R_c}\int_0^{2\pi}\overline{\rho}(x,r,\theta)\left[\overline{u}^2(x,r,\theta)\right]\mathrm{d}r\,\mathrm{d}\theta\Big/\left[\overline{\rho}_b(x)\overline{u}_b^2(x)\pi R_c^2\right]$$

$$()_b = \left[\int_0^{R_c}\int_0^{2\pi}()r\,\mathrm{d}r\,\mathrm{d}\theta\right]\Big/\left(\pi R_c^2\right) \tag{B2}$$

The calculation results under the three types of mesh are similar. In the front of the chamber, β obtained from numerical calculations remains relatively stable and is basically consistent with the theoretical solution. Because of the generation and development of turbulence downstream, β in the numerical calculation results deviates from the theoretical solution and rapidly decreases. The gap between the medium and the fine mesh is relatively small among them.
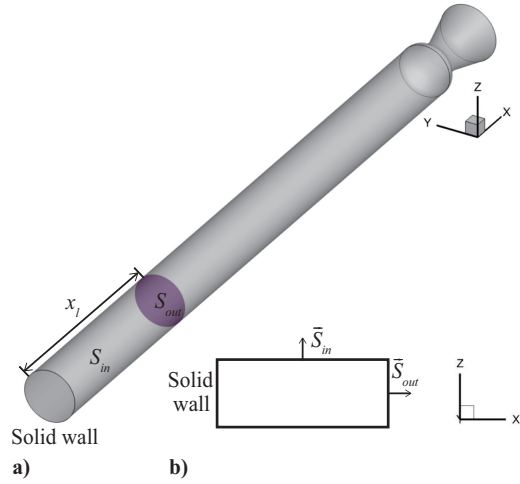
Appendix C: Verification of Mass Conservation

To further assess the numerical accuracy of the simulation, a cylindrical control volume (CV) is deployed at the front section of the chamber, where Mach is less than 0.1. As indicated by Fig. C1, the top surface of CV aligns with the solid wall of SRM, and its lateral surface aligns with the propellant grain. Consistent with fluid mechanics conventions, the normal direction of the surface is from the inside to the outside of the CV. By adjusting x_l which is the height of CV, the mass conservation in different spatial configurations can be assessed. Referring to Eq. (C1), mass change in CV $\overline{m}_{CV}(x_l)$ can be calculated through mass flux $\overline{q}_{in}(x_l)$ and $\overline{q}_{out}(x_l)$.

$$\overline{q}_{in}(x_l) = \int_{S_{in}(x_l)}\overline{\rho}\,\overline{u}_i n_i\,\mathrm{d}S \qquad \overline{q}_{out}(x_l) = \int_{S_{out}(x_l)}\overline{\rho}\,\overline{u}_i n_i\,\mathrm{d}S$$

$$\overline{m}_{CV}(x_l) = \overline{q}_{in}(x_l) + \overline{q}_{out}(x_l) \tag{C1}$$

The mass conservation is verified in three types of mesh, and the result is depicted in Fig. C2. Because the time-averaged mass within the CV is constant, condition $\overline{m}_{CV}(x_l) \to 0$ should be met. Only the simulation using fine mesh adequately satisfies the aforementioned

Fig. C1 a) Three-dimensional visualization of the control volume (CV) in SRM. b) Normal vector of surface.
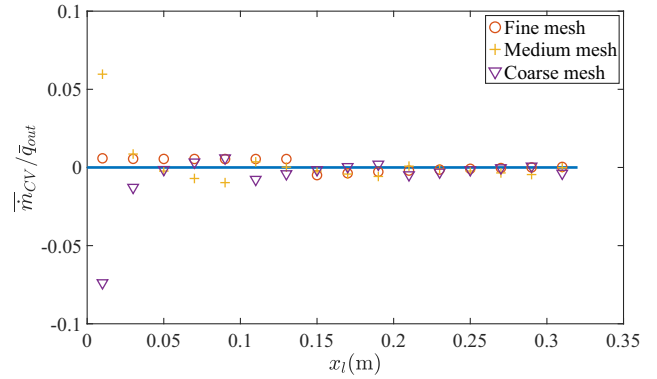
Fig. C2 Verification of mass conservation in three types of mesh.

condition. So, the fine mesh is selected for simulation to achieve better accuracy.

Appendix D: Accuracy Verification

The Taylor–Culick solution shows the theoretical velocity field in the cylindrical chamber with lateral injection is applied to validate the accuracy of the simulation calculated with fine mesh. Figure D1 shows the mean axial and radial velocity simulation and theoretical results at different stations. Because the flow gradually transitions to turbulence downstream, data from five stations are selected for comparison. The time-averaged velocity distribution in the numerical calculation results is close to the theoretical results, which validates the accuracy of the simulation.

Appendix E: Algorithm of RVMD [37]

The complete conputational strategy of RVMD is presented in this section. We use $(\cdot)^T$ to denote the transpose, $(\cdot)^*$ to denote the conjugate, and $(\cdot)^H$ to denote the conjugate transpose of matrices and vectors. The definitions of some important intermediate variables are as follows:
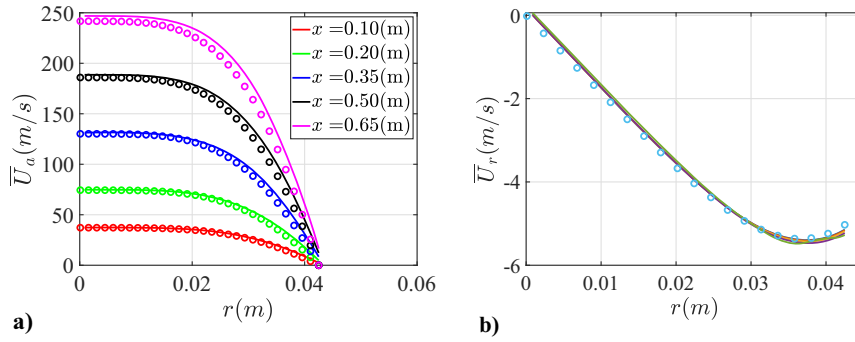
$$\varpi_i = if_s/T, i = 0, 1, 2, \ldots, T/2$$

f_s is the sampling frequency and T is the number of snapshots.

$$\hat{g}_{k,i}^n = 1/[1 + 2\alpha(\varpi_i - f_k^n)^2], i = 0, 1, 2, \ldots, T/2$$

$$W = \mathrm{diag}(\varpi)$$

$$\hat{G}_k^n = \mathrm{diag}(\hat{g}_k^n)$$

$$\hat{c} = \mathcal{F}\{c\} \quad \mathcal{F} \text{ is Fourier transform} \tag{E1}$$

Fig. D1 Comparison of a) mean axial velocity and b) mean radial velocity from simulation (lines) at various axial location with the Taylor–Culick solution (symbols).

The outline of the algorithm is as follows:
1) Set iteration step $0 \to n$, and initialize $\{\phi_k, c_k, f_k\}|_{k=1}^{K}$.
2) Loop:

from $k = 1$ to K do:

a) update the residual matrix for the kth mode using

$$\hat{R}_k^n = \hat{Q} - \sum_{i=1}^{k-1} \phi_i^{n+1} \hat{c}_i^{n+1,T} - \sum_{i=k+1}^{K} \phi_{\text{in}} \hat{c}_i^{n,T} \quad (E2)$$

b) update the spatial mode using

$$\phi_k^{n+1} = \frac{Re\{\hat{R}_k^n \hat{c}_k^{n,*}\}}{\|Re\{\hat{R}_k^n \hat{c}_k^{n,*}\}\|} \quad (E3)$$

c) update the Fourier transform of the time-evolution coefficient using

$$\hat{c}_k^{n+1} = \hat{G}_k^n \hat{R}_k^{n,T} \phi_k^{n+1} \quad (E4)$$

d) update the central frequency using

$$f_k^{n+1} = \frac{\hat{c}_k^{n+1,H} W \hat{c}_k^{n+1}}{\hat{c}_k^{n+1,H} \hat{c}_k^{n+1}} \quad (E5)$$

Set $n + 1 \to n$, and exit the loop when the following criteria is met:

$$\sum_{k=1}^{K} \frac{\|u_k^{n+1} - u_k^n\|_F^2}{\|u_k^n\|_F^2} \le \varepsilon \qquad u_k^i = \phi_k^i c_k^i \quad (E6)$$

3) Reconstruct the time-evolution coefficient c_k from $\hat{c}_k$ using the Hermitian symmetry and inverse Fourier transform to obtain the RVMD modes.

A MATLAB program for RVMD is available at https://github.com/ZimoLiao/rvmd.

Acknowledgment

References

[1] Blomshield, F., "Lessons Learned in Solid Rocket Combustion Instability," *43rd AIAA/ASME/SAE/ASEE Joint Propulsion Conference & Exhibit*, AIAA Paper 2007-5803, 2007.
https://doi.org/10.2514/6.2007-5803

[2] Cai, W., Yang, V., and Flandro, G., "Turbulent Transport in Rocket Motor Unsteady Flowfield," *Solid Propellant Chemistry, Combustion, and Motor Interior Ballistics*, Vol. 185, July 2000, pp. 837–858.
https://doi.org/10.2514/5.9781600866562.0837.0858

[3] Fabignon, Y., Dupays, J., Avalon, G., Vuillot, F., Lupoglazoff, N., Casalis, G., and Prévost, M., "Instabilities and Pressure Oscillations in Solid Rocket Motors," *Aerospace Science and Technology*, Vol. 7,

No. 3, 2003, pp. 191–200.
https://doi.org/10.1016/S1270-9638(02)01194-X

[4] Apte, S., and Yang, V., "Unsteady Flow Evolution and Combustion Dynamics of Homogeneous Solid Propellant in a Rocket Motor," *Combustion and Flame*, Vol. 131, Nos. 1–2, 2002, pp. 110–131.
https://doi.org/10.1016/S0010-2180(02)00397-8

[5] Kourta, A., "Computation of Vortex Shedding in Solid Rocket Motors Using Time-Dependent Turbulence Model," *Journal of Propulsion and Power*, Vol. 15, No. 3, 1999, pp. 390–400.
https://doi.org/10.2514/2.5457

[6] Lupoglazoff, N., and Vuillot, F., "Parietal Vortex Shedding as a Cause of Instability for Long Solid Propellant Motors-Numerial Simulations and Comparisons with Firing Tests," *34th Aerospace Sciences Meeting and Exhibit*, AIAA Paper 1996-0761, 1996.
https://doi.org/10.2514/6.1996-761

[7] Avalon, G., Ugurtas, B., Grisch, F., and Bresson, A., "Numerical Computations and Visualization Tests of the Flow Inside a Cold Gas Simulation with Characterization of a Parietal Vortex Shedding," *36th AIAA/ASME/SAE/ASEE Joint Propulsion Conference and Exhibit*, AIAA Paper 2000-3387, 2000.
https://doi.org/10.2514/6.2000-3387

[8] Lupoglazoff, N., and Vuillot, F., "Numerical Simulations of Parietal Vortex-Shedding Phenomenon in a Cold Flow Set-Up," *34th AIAA/ASME/SAE/ASEE Joint Propulsion Conference and Exhibit*, AIAA Paper 1998-3220, 1998.
https://doi.org/10.2514/6.1998-3220

[9] Gazanion, B., Chedevergne, F., and Casalis, G., "Large Eddy Simulation of the Laminar-Turbulent Transition in the Flow Induced by Wall Injection," *Procedia IUTaM*, Vol. 14, July 2015, pp. 438–447.
https://doi.org/10.1016/j.piutam.2015.03.072

[10] Avalon, G., and Lambert, D., "Cold Gas Experiments Applied to the Understanding of Aeroacoustic Phenomena Inside Solid Propellant Boosters," *42nd AIAA/ASME/SAE/ASEE Joint Propulsion Conference & Exhibit*, AIAA Paper 2006-5111, 2006.
https://doi.org/10.2514/6.2006-5111

[11] Gazanion, B., Chedevergne, F., and Casalis, G., "On the Laminar-Turbulent Transition in Injection-Driven Porous Chambers," *Experiments in Fluids*, Vol. 55, Dec. 2014, pp. 1–13.
https://doi.org/10.1007/s00348-013-1643-y

[12] Apte, S., and Yang, V., "Unsteady Flow Evolution in Porous Chamber with Surface Mass Injection, Part 1: Free Oscillation," *AIAA Journal*, Vol. 39, No. 8, 2001, pp. 1577–1586.
https://doi.org/10.2514/2.1483

[13] Li, Y., Wang, Z., Liu, P., He, W., and Li, L. K., "A Theoretical Study of Parietal Vortex Shedding in Taylor–Culick Flow via Linear Stability Analysis," *Physics of Fluids*, Vol. 32, No. 10, 2020.
https://doi.org/10.1063/5.0025417

[14] Dotson, K., Koshigoe, S., and Pace, K., "Vortex Shedding in a Large Solid Rocket Motor Without Inhibitors at the Segment Interfaces," *Journal of Propulsion and Power*, Vol. 13, No. 2, 1997, pp. 197–206.
https://doi.org/10.2514/2.5170

[15] Rossiter, J., "Wind-Tunnel Experiments on the Flow over Rectangular Cavities at Subsonic and Transonic Speeds," Aeronautical Research Council R&M TR 3438, 1964, https://reports.aerade.cranfield.ac.uk/handle/1826.2/4020.

[16] Flandro, G., and Jacobs, H., "Vortex Generated Sound in Cavities," *Aeroacoustics Conference*, AIAA Paper 1973-1014, 1973.
https://doi.org/10.2514/6.1973-1014

[17] LUPOGLAZOFF, N., and Vuillot, F., "Numerical Simulation of Vortex Shedding Phenomenon in 2D Test Case Solid Rocket Motors," *30th Aerospace Sciences Meeting and Exhibit*, AIAA Paper

1992-0776, 1992.
https://doi.org/10.2514/6.1992-776

[18] Vuillot, F., and Lupoglazoff, N., "Combustion and Turbulent Flow Effects in 2D Unsteady Navier-Stokes Simulations of Oscillatory Solid Rocket Motors-First Applications," *34th Aerospace Sciences Meeting and Exhibit*, AIAA Paper 1996-0884, 1996.
https://doi.org/10.2514/6.1996-884

[19] Najjar, F., Ferry, J., Wasistho, B., and Balachandar, S., "Full-Physics Large-Scale Multiphase Large Eddy Simulations of Flow Inside Solid Rocket Motors," *38th AIAA/ASME/SAE/ASEE Joint Propulsion Conference & Exhibit*, AIAA Paper 2002-4343, 2002.
https://doi.org/10.2514/6.2002-4343

[20] Lupoglazoff, N., and Vuillot, F., "Comparison Between Firing Tests and Numerical Simulation of Vortex Shedding in a 2-D Test Solid Motor," *23rd Fluid Dynamics, Plasmadynamics, and Lasers Conference*, AIAA Paper 1993-3066, 1993.
https://doi.org/10.2514/6.1993-3066

[21] Wasistho, B., and Moser, R., "Simulation Strategy of Turbulent Internal Flow in Solid Rocket Motor," *Journal of Propulsion and Power*, Vol. 21, No. 2, 2005, pp. 251–263.
https://doi.org/10.2514/1.7760

[22] Bernardini, M., Cimini, M., Stella, F., Cavallini, E., Di Mascio, A., Neri, A., and Martelli, E., "Large-Eddy Simulation of Vortex Shedding and Pressure Oscillations in Solid Rocket Motors," *AIAA Journal*, Vol. 58, No. 12, 2020, pp. 5191–5201.
https://doi.org/10.2514/1.J058866

[23] Apte, S., and Yang, V., "Turbulent Flame Dynamics of Homogeneous Solid Propellant in a Rocket Motor," *Proceedings of the Combustion Institute*, Vol. 28, No. 1, 2000, pp. 903–910.
https://doi.org/10.1016/S0082-0784(00)80296-9

[24] Apte, S., and Yang, V., "A Large-Eddy Simulation Study of Transition and Flow Instability in a Porous-Walled Chamber with Mass Injection," *Journal of Fluid Mechanics*, Vol. 477, March 2003, pp. 215–225.
https://doi.org/10.1017/S0022112002002987

[25] Di Mascio, A., Martelli, E., Bernardini, M., Stella, F., and Neri, A., "Boundary Conditions for Inhomogeneous Combustion Simulation in Solid Rocket Motors," *AIAA Journal*, Vol. 61, No. 5, 2023, pp. 2314–2318.
https://doi.org/10.2514/1.J062554

[26] Tsinober, A., *An Informal Conceptual Introduction to Turbulence*, Springer, Berlin, 2009.
https://doi.org/10.1007/0-306-48384-x

[27] Holmes, P., *Turbulence, Coherent Structures, Dynamical Systems and Symmetry*, Cambridge Univ. Press, Cambridge, England, U.K., 2012.
https://doi.org/10.1017/CBO9780511919701

[28] Taira, K., Hemati, M. S., Brunton, S. L., Sun, Y., Duraisamy, K., Bagheri, S., Dawson, S. T., and Yeh, C.-A., "Modal Analysis of Fluid Flows: Applications and Outlook," *AIAA Journal*, Vol. 58, No. 3, 2020, pp. 998–1022.
https://doi.org/10.2514/1.J058462

[29] Lumley, J. L., "The Structure of Inhomogeneous Turbulent Flows," *Atmospheric Turbulence and Radio Wave Propagation*, Nauka, Moscow, RU, 1967, pp. 166–178.

[30] Schmid, P. J., "Dynamic Mode Decomposition of Numerical and Experimental Data," *Journal of Fluid Mechanics*, Vol. 656, July 2010, pp. 5–28.
https://doi.org/10.1017/S0022112010001217

[31] Taira, K., Brunton, S. L., Dawson, S. T., Rowley, C. W., Colonius, T., McKeon, B. J., Schmidt, O. T., Gordeyev, S., Theofilis, V., and Ukeiley, L. S., "Modal Analysis of Fluid Flows: An Overview," *AIAA Journal*, Vol. 55, No. 12, 2017, pp. 4013–4041.
https://doi.org/10.2514/1.J056060

[32] Muld, T. W., Efraimsson, G., and Henningson, D. S., "Flow Structures Around a High-Speed Train Extracted Using Proper Orthogonal Decomposition and Dynamic Mode Decomposition," *Computers & Fluids*, Vol. 57, Jan. 2012, pp. 87–97.
https://doi.org/10.1016/j.compfluid.2011.12.012

[33] Schmid, P. J., Meyer, K. E., and Pust, O., "Dynamic Mode Decomposition and Proper Orthogonal Decomposition of Flow in a Lid-Driven Cylindrical Cavity," *8th International Symposium on Particle Image Velocimetry*, Springer, Heidelberg, Germany, 2009, pp. 25–28.
https://api.semanticscholar.org/CorpusID:126049714.

[34] Tu, J. H., "Dynamic Mode Decomposition: Theory and Applications," Ph.D. Thesis, Princeton Univ., Princeton, NJ, 2013, https://www.proquest.com/openview/7a0ee5515e356a31e8eb3ebb3772414c/1?pq-origsite=gscholarcbl=18750.

[35] Gilka, G., Luchtenburg, D. M., Thiele, F., and Morzynski, M., "Dynamic Characterization of an Actuated Bluff Body Wake," *V European Conference on Computational Fluid Dynamics, ECCO-*

MAS CFD, Springer, Heidelberg, Germany, 2010, pp. 1–17, https://www.researchgate.net/publication/262674283_Dynamic_characterization_of_an_actuated_bluff_body_wake.

[36] Li, W., Zhao, D., Zhang, L., and Chen, X., "Proper Orthogonal and Dynamic Mode Decomposition Analyses of Nonlinear Combustion Instabilities in a Solid-Fuel Ramjet Combustor," *Thermal Science and Engineering Progress*, Vol. 27, Dec. 2022, Paper 101147.
https://doi.org/10.1016/j.tsep.2021.101147

[37] Liao, Z.-M., Zhao, Z., Chen, L.-B., Wan, Z.-H., Liu, N.-S., and Lu, X.-Y., "Reduced-Order Variational Mode Decomposition to Reveal Transient and Non-Stationary Dynamics in Fluid Flows," *Journal of Fluid Mechanics*, Vol. 966, June 2023, Paper A7.
https://doi.org/10.1017/jfm.2023.435

[38] Kundu, P. K., Cohen, I. M., and Dowling, D. R., *Fluid Mechanics*, 6th ed., Academic Press, New York, 2016.
https://doi.org/10.1016/C2012-0-00611-4

[39] Nicoud, F., and Ducros, F., "Subgrid-Scale Stress Modelling Based on the Square of the Velocity Gradient Tensor," *Flow, Turbulence and Combustion*, Vol. 62, No. 3, 1999, pp. 183–200.
https://doi.org/10.1023/A:1009995426001

[40] Huang, N. E., Shen, Z., Long, S. R., Wu, M. C., Shih, H. H., Zheng, Q., Yen, N.-C., Tung, C. C., and Liu, H. H., "The Empirical Mode Decomposition and the Hilbert Spectrum for Nonlinear and Non-Stationary Time Series Analysis," *Proceedings of the Royal Society of London. Series A: Mathematical, Physical and Engineering Sciences*, Vol. 454, No. 1971, 1998, pp. 903–995.
https://doi.org/10.1098/rspa.1998.0193

[41] Daubechies, I., Lu, J., and Wu, H.-T., "Synchrosqueezed Wavelet Transforms: An Empirical Mode Decomposition-Like Tool," *Applied and Computational Harmonic Analysis*, Vol. 30, No. 2, 2011, pp. 243–261.
https://doi.org/10.1016/j.acha.2010.08.002

[42] Gilles, J., "Empirical Wavelet Transform," *IEEE Transactions on Signal Processing*, Vol. 61, No. 16, 2013, pp. 3999–4010.
https://doi.org/10.1109/TSP.2013.2265222

[43] Boyd, S., Parikh, N., Chu, E., Peleato, B., Eckstein, J., et al., "Distributed Optimization and Statistical Learning via the Alternating Direction Method of Multipliers," *Foundations and Trends in Machine Learning*, Vol. 3, No. 1, 2011, pp. 1–122.
https://doi.org/10.1561/2200000016

[44] Dragomiretskiy, K., and Zosso, D., "Variational Mode Decomposition," *IEEE Transactions on Signal Processing*, Vol. 62, No. 3, 2013, pp. 531–544.
https://doi.org/10.1109/TSP.2013.2288675

[45] Lei, Y., "Signal Processing and Feature Extraction," *Intelligent Fault Diagnosis and Remaining Useful Life Prediction of Rotating Machinery*, Butterworth-Heinemann, Oxford, U.K., 2017, pp. 17–66.
https://doi.org/10.1016/B978-0-12-811534-3.00002-0

[46] Dunlap, R., Blackner, A., Waugh, R., Brown, R., and Willoughby, P., "Internal Flow Field Studies in a Simulated Cylindrical Port Rocket Chamber," *Journal of Propulsion and Power*, Vol. 6, No. 6, 1990, pp. 690–704.
https://doi.org/10.2514/3.23274

[47] Hunt, J. C., Wray, A. A., and Moin, P., "Eddies, Streams, and Convergence Zones in Turbulent Flows," *Studying Turbulence Using Numerical Simulation Databases, 2. Proceedings of the 1988 Summer Program*, NASA, Paper 19890015184, 1988, https://ntrs.nasa.gov/citations/19890015184.

[48] Bernardini, M., and Pirozzoli, S., "Wall Pressure Fluctuations Beneath Supersonic Turbulent Boundary Layers," *Physics of Fluids*, Vol. 23, No. 8, 2011.
https://doi.org/10.1063/1.3622773

[49] Culick, F., Magiawala, K., et al., "Excitation of Acoustic Modes in a Chamber by Vortex Shedding," *Journal of Sound and Vibration*, Vol. 64, No. 3, 1979, pp. 455–457.
https://doi.org/10.1016/0022-460X(79)90591-1

[50] Dunlap, R., and Brown, R., "Exploratory Experiments on Acoustic Oscillations Driven by Periodic Vortex Shedding," *AIAA Journal*, Vol. 19, No. 3, 1981, pp. 408–409.
https://doi.org/10.2514/3.7783

[51] Wilmarth, W., "Pressure Fluctuations Beneath Turbulent Boundary Layers," *Annual Review of Fluid Mechanics*, Vol. 7, Jan. 1975, pp. 13–36.
https://doi.org/10.1146/annurev.fl.07.010175.000305

[52] Wills, J., "On Convection Velocities in Turbulent Shear Flows," *Journal of Fluid Mechanics*, Vol. 20, No. 3, 1964, pp. 417–432.
https://doi.org/10.1017/S002211206400132X

[53] Rockwell, D., "Oscillations of Impinging Shear Layers," *AIAA Journal*, Vol. 21, No. 5, 1983, pp. 645–664.
https://doi.org/10.2514/3.8130

[54] Powell, A., "On the Mechanism of Choked Jet Noise," *Proceedings of the Physical Society. Section B*, Vol. 66, No. 12, 1953, p. 1039.
https://doi.org/10.1088/0370-1301/66/12/306

[55] Berman, A. S., *Laminar Flow in Channels with Porous Walls*, Vol. 944, Carbide and Carbon Chemicals Company, K-25 Plant, Oak Ridge, TN, 1952.
https://doi.org/10.1016/0300-9467(89)80087-5

[56] Taylor, G. I., "Fluid Flow in Regions Bounded by Porous Surfaces," *Proceedings of the Royal Society of London. Series A. Mathematical and Physical Sciences*, Vol. 234, No. 1199, 1956, pp. 456–475.
https://doi.org/10.1098/rspa.1956.0050

[57] Culick, F., "Rotational Axisymmetric Mean Flow and Damping of Acoustic Waves in Asolid Propellant Rocket," *AIAA Journal*, Vol. 4, No. 8, 1966, pp. 1462–1464.
https://doi.org/10.2514/3.3709

[58] Wageman, W., and Guevara, F., "Fluid Flow Through a Porous Channel," *Physics of Fluids*, Vol. 3, No. 6, 1960, pp. 878–881.
https://doi.org/10.1063/1.1706151

[59] Yamada, K., Goto, M., and Ishikawa, N., "Simulative Study on the Erosive Burning of Solid Rocket Motors," *AIAA Journal*, Vol. 14, No. 9, 1976, pp. 1170–1176.
https://doi.org/10.2514/3.61451

[60] Dunlap, R., Willoughby, P., and Hermsen, R., "Flowfield in the Combustion Chamber of a Solid Propellant Rocket Motor," *AIAA Journal*, Vol. 12, No. 10, 1974, pp. 1440–1442.
https://doi.org/10.2514/3.49513

[61] Beddini, R. A., "Injection-Induced Flows in Porous-Walled Ducts," *AIAA Journal*, Vol. 24, No. 11, 1986, pp. 1766–1773.
https://doi.org/10.2514/3.9522

[62] Larsson, J., and Lele, S. K., "Direct Numerical Simulation of Canonical Shock/Turbulence Interaction," *Physics of Fluids*, Vol. 21, No. 12, 2009.
https://doi.org/10.1063/1.3275856

K. Taira
Associate Editor